Strong optomechanical interactions with long-lived fundamental acoustic waves

Wendao Xu,[1,*] Arjun Iyer,[1] Lei Jin,[2] Sze Y. Set,[2] AND William H. Renninger[1]

[1]Institute of Optics, University of Rochester, Rochester, New York 14627, USA
[2]Research Center for Advanced Science and Technology, University of Tokyo, Tokyo 153-8904, Japan
**Corresponding author: wxu21@ur.rochester.edu*

Traveling-wave optomechanical interactions, known as Brillouin interactions, have now been established as a powerful and versatile resource for photonic sources, sensors, and radio-frequency processors. However, established Brillouinbased interactions with sufficient interaction strengths involve short phonon lifetimes, which critically limit their performanceforapplications,includingradio-frequencyfilteringandoptomechanicalstoragedevices.Here,weinvestigate a new paradigm of optomechanical interactions with tightly confined fundamental acoustic modes, which enables the unique and desirable combination of high optomechanical coupling, long phonon lifetimes, tunable phonon frequencies, and single-sideband amplification. Using sensitive four-wave mixing spectroscopy controlling for noise and spatial mode coupling, optomechanical interactions with long >2 μs phonon lifetimes and strong >400 $\mathrm{W}^{-1}\,\mathrm{m}^{-1}$ coupling are observed in a tapered fiber. In addition, we demonstrate novel phonon self-interference effects resulting from the unique combination of an axially varying device geometry with long phonon lifetimes. A generalized theoretical model, in excellent agreement with experiments, is developed with broad applicability to inhomogeneous optomechanicalsystems.

INTRODUCTION

Stimulated Brillouin scattering, a coherent interaction between optical and acoustic waves, has now been established as a powerful resource for photonic applications [1,2] including laser oscillators [3–6], RF signal generators [7,8], and distributed environmental sensors [9,10]. These applications desire large optomechanical (optical-acoustical) interaction strengths to improve pump efficiency, microwave signal strength, and sensitivity, as well as to enable smaller footprints. In addition to large coupling strengths, applications including microwave filters [11–14], optical delay, andstoragedevices[15–21]benefitfrominteractionswithacoustic waves with long phonon lifetimes by improving filter resolutions, delay periods, and storage times. However, as detailed in the following paragraph, Brillouin-active devices to date have an inverse relationship between interaction strength and phonon lifetime, and it is currently challenging to achieve large coupling and long phononlifetimesinthesameplatform.

Thewell-establishedtraditionalbackwardBrillouininteraction [22–24], for example, has a large optomechanical interaction strengthbecausetheopticalandacousticfieldsarewelloverlapped. However, the interaction between two counter-propagating optical fields requires phonons with high, GHz frequencies and correspondingly low lifetimes (~10 ns). On the other hand, Brillouininteractionsbetweencopropagatingopticalfieldsinoptical fibers [25,26] involve higher-order acoustic mode families with lower frequencies in the MHz range and correspondingly longer lifetimes. However, these interactions suffer from weak interaction strengths due to a mismatch in the transverse size of the participating optical and acoustic modes. Finally, more recent forward Brillouin interactions in photonic crystal fibers [27] and integrated Brillouin devices achieve much larger coupling strengths [28–31] by tightly confining participating fields. However, this tightconfinementyieldshighfrequencies(GHz)withcorrespondingly short phonon lifetimes because of the inverse relationship betweenthefrequencyandthewaveguidecross-sectionsizesforthe participatinghigherorderacousticmodefamily.

This research focuses instead on the fundamental acoustic modes, which exist at all frequencies in bulk and waveguide systems and do not have the lower frequency bound that limits the higher-order acoustic modes [32]. The fundamental acoustic waves enable lower acoustic frequencies with correspondingly longer lifetimes but without sacrificing the tight confinement that enables strong interactions. Forward intermodal Brillouin interactions can couple to the fundamental acoustic modes with the frequency of interaction determined by the tunable relative effective indices of the participating optical modes instead of the fixed geometry. While there is a brief report using the fundamental flexural mode to mediate forward intermodal scattering in twomode fibers in 1990 [33], the interaction strength, as with other early demonstrations of forward Brillouin [25], was limited by the use of standard fiber geometries, in which the light in the fiber core has a very small overlap with the acoustic mode extending out through the cladding. Note that Brillouin-based microresonators [34–36] can also access lower frequencies and correspondingly longer acoustic lifetimes, but with lower equivalent traveling-wave Brillouin gain [37] and additional practical complications associated with the optical and acoustic frequency modal restrictions inherent with resonators. In traveling-wave systems, novel device design techniques are required to achieve strong confinement of acoustic waves with the long wavelengths needed for large phonon lifetimes. However, if strong optical coupling can be achieved with the frequency-agile fundamental acoustic modes, this versatile optomechanical interaction would enable unprecedented access to simultaneousstrongcouplingandlonglifetimes.

Here, we demonstrate strong **F**orward **I**nter-**M**odal Brillouin interactions with the **F**undamental **A**coustic **M**odes (**FIM-FAM**) of an optomechanical fiber taper. The fundamental flexural acoustic mode of an exponential fiber taper couples light optomechanically between two of the lowest order optical spatial modes of the taper. The tight confinement enabled by the fiber-air boundary of the taper provides an ideal optomechanical overlap yielding Brillouin coupling strengths >400 W^{-1} m^{-1}, which is the strongest observed to date from a fiber taper [38,39] and is comparable to the largest optomechanical coupling strength for any system. Moreover, the corresponding fundamental flexural acoustic mode participating in this interaction has much longer measured lifetimes >2 μs than obtained in other high-gain traveling-wave Brillouin systems, enabling a record combination of coupling strengths and phonon lifetimes. While interactions of this type have been investigated recently numerically [40], no experiments have been reported to date. In addition, because of this new parameter regime for optomechanical interactions, novel phonon self-interference phenomena are observed for the first time. We detail how phonon self-interference arises from axial variations in the acoustic waveguide that occur within the range of the uniquely long phonon decay length. We derive a generalized theoretical framework modeling phonon self-interference in excellent agreement with experimental results. The strong FIM-FAM optomechanical interactions presented here provide promising opportunities for tailorable coupling to previously inaccessible frequency regimes and phonon lifetimes and will be desirable for establishedandemergingoptomechanicaltechnologies.

1. FIM-FAM INTERACTIONS IN A FIBER TAPER

FIM-FAM interactions are considered here in a few-mode fiber optical taper (Fig. 1). FIM-FAM is a coherent optomechanical process through which a fundamental acoustic mode with frequency⍰andwavevector$q$ mediatesparametriccouplingbetween two distinct optical spatial modes (pump with frequency ω_p and wavevector β_p, and Stokes with frequency ω_s and wavevector β_s). For coupling to occur, the interaction must satisfy phase matching ($1\beta = \beta_p - \beta_s = q$) and energy conservation (⍰ = $\omega_p - \omega_s$). These conditions can be succinctly expressed graphically by examining the acoustic dispersion lines [q(⍰)] and the difference in opticalwavevectorsbetweenthetwoopticalmodes,1β [Fig.1(b)]. In this picture, interactions are possible at the frequencies where these lines intersect. Intermodal Brillouin interactions of this type allow for stimulated gain, single-sideband amplification, and nonreciprocal processes because of distinct phonon modes mediating Stokes and anti-Stokes processes [26,41,42]. In addition, because the interaction frequency is determined by 1β, by engineering the differential effective index of the participating optical modes, 1β, the frequency of the interaction, ⍰, can be tuned. However, as illustrated in Fig. 1(b), when changing 1β for the higher order modes [magenta lines in Fig. 1(b)] that are the subject of previous studies of intermodal Brillouin scattering [30,43], the frequency remains close to its q = 0 value, which is fixed by the geometry. In contrast, with the fundamental acoustic modes [cyan lines in Fig. 1(b)], there is no low-frequency cutoff, and all frequencies become available. FIM-FAM, therefore, offers a wide new window ofopportunityfortraveling-waveoptomechanicalinteractions.

For FIM-FAM, distinct optical modes are required to mediate intermodalinteractions.Lightisconfinedinthewaistoftheoptical taper through total internal reflection at the air-glass boundary. The optical modes are calculated by modeling the fiber taper as a uniform silica cylinder between two transition regions [Fig. 2(a)]. TheBrillouin-activewaistregion[blueinFig.2(a)]ischaracterized by diameter d and length L. The number of optical modes supportedbythisstructureisdeterminedbythenormalizedfrequency, $V = \frac{2\pi r}{\lambda}\sqrt{n_s^2 - n_a^2}$,where$r$ =$d/2$isthetaperradius,λistheopticalwavelength,n_s istherefractiveindexoffusedsilica,andn_a isthe refractive index of air. The dispersion curves for the optical modes

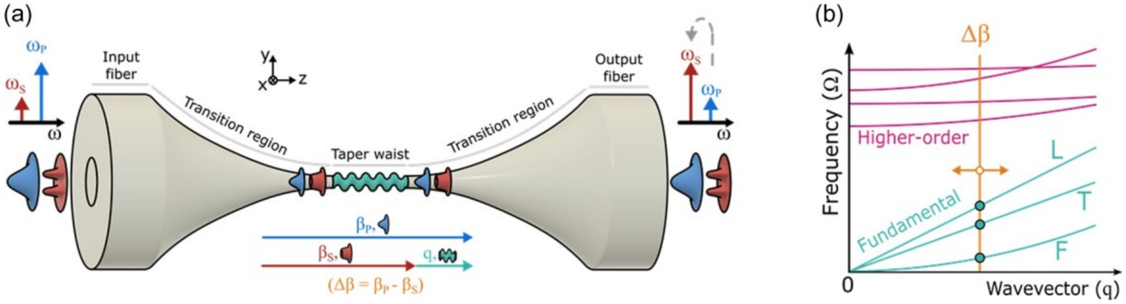

Fig. 1. Taper-based FIM-FAM device. (a) An illustration of the FIM-FAM process in a few-mode taper. Regions of the taper are labeled above each section. Pump (ω_P) and Stoke (ω_S) beams input respectively into the fundamental and higher-order spatial modes of the input fiber core couple through the transition region into the fundamental mode and higher-order mode family of the taper waist, where the pump light is optomechanically coupled to the Stokes field through the FIM-FAM process before being coupled out of the device in the two modes of the output fiber core through the second transition region. The phase-matching relations for the FIM-FAM interaction indicating the optical wavevector difference between the axial wavevector of the two participating optical modes, 1β, must equal the acoustic wavevector, q, is inset below the device. (b) The acoustic dispersion profiles for the modes of the taper waist. While the higher-order acoustic modes (magenta) have a fixed nonzero cutoff frequency at q = 0, the fundamental mode frequencies (⍰) and wavevectors (q) extend continuously to zero (cyan). Optomechanical interactions are possible at frequencies where the optical wavevector difference (1β) intersects the acoustic dispersion curves. In contrast to interactions with the higher-order modes, FIM-FAM interactions with the fundamental modes can betunedinfrequencybyvaryingtheopticalwavevectordifference,1β.

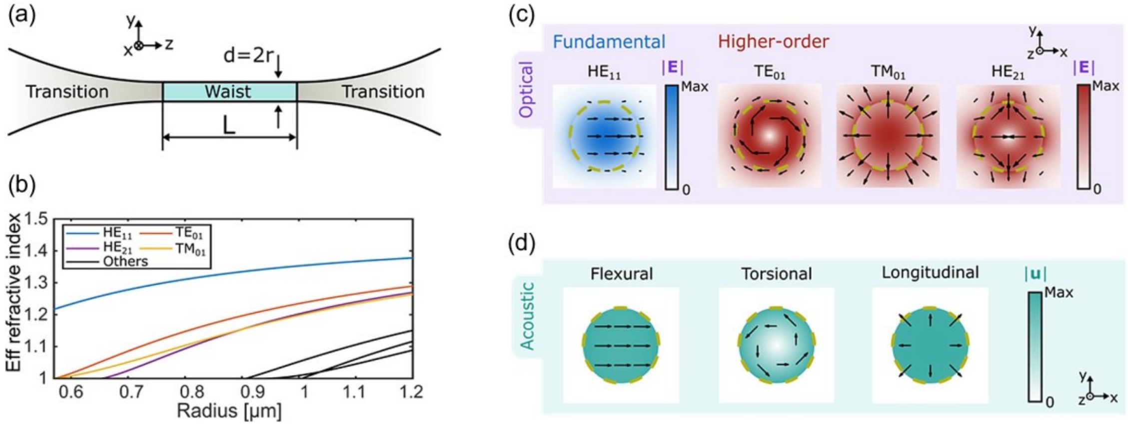

Fig. 2. Optical and acoustic modes of the fiber taper. (a) The optomechanical modes of the taper waist are calculated assuming a uniform cylinder with length (L) and diameter ($d = 2r$, for radius r). (b) The effective refractive index of the optical modes as a function of taper radius. (c) Electric field distributions of the first four optical modes, which participate in the FIM-FAM process under consideration. (d) Displacement profiles of the fundamental acoustic modes confined in the taper waist. The glass-air boundary is indicated with dashed circles.

are calculated using a standard step-index waveguide analysis [44] for the waist as a function of radius [Fig. 2(b)]. Constraining the taper radius to between 570 and 900 nm ensures that exactly two optical mode families are guided in the waist of the taper: the fundamental mode (HE_{11}), and three higher-order modes (TE_{01}, TM_{01}, and HE_{21} for $r > 650$ nm). The spatial electric field distribution for the fundamental and the higher order optical modes is illustrated in Fig. 2(c).

The acoustic modes are also strongly confined in the fiber taper by the large acoustic impedance mismatch between silica and air. The acoustic modes are calculated by solving the acoustic Pochhammer-Chree equations [45–49] for a uniform cylinder of silica. The acoustic modes (guided acoustic phonons) of the taper can be broadly categorized into three mode families, named after their unique displacement profiles: the flexural, torsional, and longitudinal (axial-radial) modes. The fundamental acoustic modes (FAMs) are defined as the lowest frequency mode from each mode family, with all other modes referred to as higher order modes. The spatial displacement profiles of the three fundamental acoustic modes in the taper waist are illustrated in Fig. 2(d). The dispersion for both families of the acoustic modes is calculated for the experimentally relevant taper waist radius of $r = 830$ nm [Fig. 3(a)]. Finite-element model calculations validated by analytic solutions reproduce the dispersion curves and enable this analysis to be extended to more complicated geometries.

FIM-FAM coupling strength can now be quantified through the vectorial overlap [50] of the optical forces with the acoustic mode displacement. The relevant optical forces are electrostriction within the taper, and electrostriction and radiation pressure on the surface of the taper. While nonzero coupling is found for a variety of combinations of optical and acoustic modes, for the lowest order optical and acoustic modes calculated above (e.g., in Fig. 2), the strongest interactions occur between the fundamental optical mode (HE_{11}), one other higher order optical mode (TE_{01}, TM_{01}, or HE_{21}), and the fundamental flexural acoustic mode. The differential index, $\boldsymbol{1\beta}$, between the fundamental optical mode and each of the three higher order optical modes is plotted with the acoustic dispersion curves indicating three distinct optomechanical interactions with the fundamental flexural acoustic mode [Fig. 3(a)]. Using the calculated optical forces for each of the three higher order optical modes [Fig. 3(b)] and the fundamental flexural acoustic mode with an assumed linear polarization in the x-direction [Fig. 3(b)], the total coupling strength this found to be 428, 532, and 347 W^{-1} m^{-1} for acoustic frequencies 134, 209, and 220 MHz, through interactions with higher order optical modes TE_{01}, TM_{01}, and HE_{21}, respectively. Note that the three optical forcing mechanisms play comparable roles, and the interference between the forces is substantial [Fig. 3(c)]. For example, the electrostrictive surface forces counteract radiation pressure and electrostriction within this taper [note the sign of the integrated contributions in Fig. 3(c)]. The

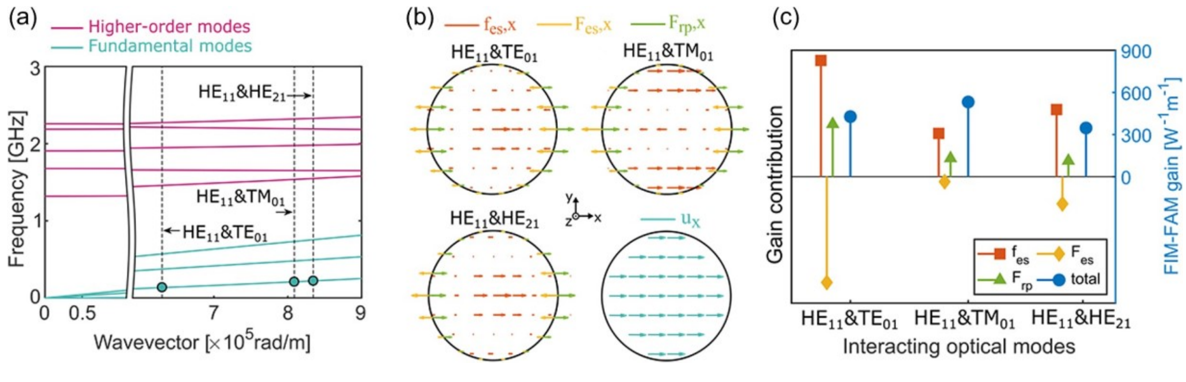

Fig. 3. Optomechanical coupling strength calculations for the FIM-FAM interaction. (a) Calculated acoustic dispersion profiles for a taper waist with $r = 830$ nm, including three fundamental (cyan) and several higher-order (magenta) acoustic modes. The optical wavevector differences between the fundamental optical mode and three higher-order modes are indicated by vertical dashed lines. (b) The spatial distribution of the relevant x-components of the optical forces (bulk electrostriction f_{es} in red, surface electrostriction F_{es} in orange, radiation pressure F_{rp} in green) for FIM-FAM interactions between the fundamental mode and each of the three higher-order modes along with the x-component of acoustic displacement of the fundamental flexural mode (cyan). (c) The relative contributions of the three optical forcing mechanisms and the combined vectorial sum giving the total FIM-FAM gain.

coupling strength is calculated assuming a quality factor of $Q = 2000$, which is typical of acoustic modes in silica at comparable frequencies [51,52]. For these FIM-FAM interactions, therefore, the phonon lifetime is long (>1 µs) with large coupling strengths > 300 $\mathrm{W^{-1}m^{-1}}$. Note that in the same taper geometry, conventional intermodal interactions with higher order acoustic modes only exist at frequencies above 1.5 GHz, highlighting the utility of FIM-FAM for accessing a wide new range of phonon frequencies with longer lifetimes than previously available.

2. RESULTS

An optical taper is fabricated from a standard few-mode optical fiber to investigate FIM-FAM. A static ceramic electrical heater is used to heat the fiber locally, while two mechanical stages pull it simultaneously at both ends. The static heater configuration yields a taper with exponential transition regions. The tapers are designed with a waist length of ∼10 mm, and a nominal radius of $r = 830$ nm to ensure two-mode operation, as described above. Additional taper fabrication details can be found in Supplement 1.

The FIM-FAM interaction is measured in the taper with a sensitive phonon-mediated four-wave mixing technique (Fig. 4). Through this process, two optical tones drive the flexural acoustic mode, and a third probe tone scatters off the driven acoustic mode to generate a fourth tone measured with heterodyne detection. A CW laser at 1550 nm (the carrier, ω_c) is amplified and divided into three fiber paths [Fig. 4(a)]. On one path, the optical field is modulated by a null-biased intensity modulator with a fixed frequency of $\omega_1 = 2\pi \times 10$ GHz, followed by a narrow fiber Bragg grating (FBG) to filter out the lower frequency sideband at $\omega_f = \omega_c - \omega_1$. The remaining higher frequency sideband serves as one of the acoustic drive tones, drive$_1$, with frequency, $\omega_{d1} = \omega_c + \omega_1$ [Fig. 4(b)]. On the second path, the carrier is first acousto-optically blue-shifted by $1 = 2\pi \times 39$ MHz for use with frequency stabilization (see Supplement 1 for more details). The blue-shifted field with frequency, $\omega_{\mathrm{AOM}} = \omega_c + 1$ is then modulated with a null-biased intensity modulator at a frequency ω_2, to generate another acoustic drive tone at a higher frequency, drive$_2$, with frequency $\omega_{d2} = \omega_{\mathrm{AOM}} + \omega_2 = \omega_c + \omega_2 + 1$, and a probe tone at a lower frequency with frequency $\omega_p = \omega_{\mathrm{AOM}} - \omega_2 = \omega_c - \omega_2 + 1$ [Fig. 4(b)]. Ω is the frequency of the acoustic wave to be driven inside the taper. ω_{d1} and ω_{d2} are chosen such that the difference between the two ($\Omega = \omega_1 - \omega_2 - 1$) can be continuously varied through targeted acoustic resonance frequencies. We can rewrite ω_2 in terms of phonon frequency Ω as $\omega_2 = \omega_1 - 1 - \Omega$.

The carrier on the third path with frequency ω_c acts as a local oscillator (LO) for heterodyne detection of the optomechanical response signal. The two acoustic drives are amplified by EDFAs to about 30–40 mW before entering the fiber taper. Two sets of polarization controllers, half-wave plates, and polarizing beam splitters are used to ensure that the fields entering the mode-selective coupler (MSC) are linearly polarized. The MSC couples the drive$_1$ field into the fundamental mode of the input port of the fiber taper. The MSC also couples drive$_2$ and the probe tones into the first higher order mode family of the taper. In the fiber taper under test, the probe tone interacts with the acoustic wave generated by the two acoustic drives separated by frequency Ω and creates the anti-Stokes (Stokes) signal at $\omega_{AS} = \omega_p + \Omega = \omega_c - \omega_1 + 21 + 2\Omega$ ($\omega_S = \omega_p - \Omega = \omega_c - \omega_1 + 21$). A single-mode collimator serves as a spatial filter after the taper, collecting the optomechanically scattered light in the fundamental mode and strongly rejecting drive$_2$ and probe light in the higher order mode family. Excess acoustic drive tones are filtered out with two FBG filters. The remaining anti-Stokes (Stokes) signal is mixed with the local oscillator at frequency, ω_c, and the resulting heterodyne beat signal is detected at $\omega_{\mathrm{het},AS} = \omega_1 - 21 - 2\Omega$ ($\omega_{\mathrm{het},S} = \omega_1 - 21$). The FIM-FAM spectra are obtained by increasing ω_2 with a fixed ω_1 to continuously decrease Ω in the targeted frequency range and implementing a lock-in measurement of the measured sideband on an electrical spectrum analyzer.

The Stokes signal downshifted in frequency from the probe can be frequency-resolved from the upshifted anti-Stokes signal, which enables the observation of nonreciprocity and single-sideband amplification. After the mode conversion by the MSC, drive$_1$ propagates in the $\mathrm{LP_{01}}$ mode into the taper, while drive$_2$ and probe

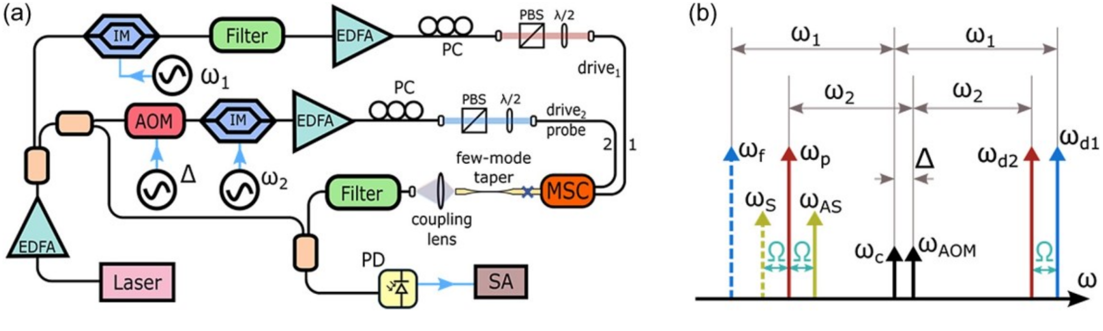

Fig. 4. FIM-FAM spectroscopy technique. (a) Experimental schematic with EDFA, erbium-doped fiber amplifier; AOM, acousto-optic modulator; IM, intensity modulator; PC, polarization controller; PBS, polarizing beam splitter; MSC, mode selective coupler; PD, photodetector; SA, spectrum analyzer; and $\lambda/2$, half-wave plate. Ports 1 and 2 of the MSC couple into the $\mathrm{LP_{01}}$ and $\mathrm{LP_{11}}$ modes into the few-mode fiber, respectively. Blue arrows represent electrical signals. (b) The salient optical frequencies: ω_c, carrier, and LO frequency; ω_{AOM}, frequency of the AOM shifted carrier; ω_1 and ω_2 are modulation frequencies applied to the intensity modulators; ω_f, optical frequency filtered by the first filter; and ω_p, the probe frequency. The acoustic wave with frequency Ω is optically excited by two acoustic drives (drive$_1$ at ω_{d1} and drive$_2$ at ω_{d2}), and the Stokes (ω_S) and anti-Stokes (ω_{AS}) sidebands are generated on either side of the probe with offset, Ω.

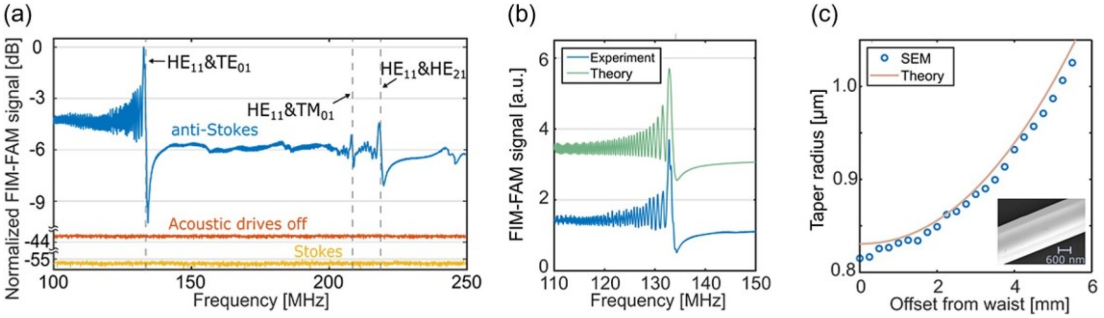

Fig.5. Experimentalresults.(a)Measuredanti-Stokesresponse(blue)oftheopticaltaperasafunctionofthedifferenceindrivefrequencies(⍰)revealing strong coupling to three FIM-FAM acoustic resonances mediated by the flexural mode. The corresponding Stokes response (yellow) and no-drive response (orange) do not yield signatures of resonant optomechanical interactions, as expected. The resonance frequencies agree very well with theoretical predictions (dashed lines), confirming FIM-FAM coupling. (b) The measured resonances exhibit oscillating spectral signatures (interaction between the HE_{11} and TE_{01} optical modes replotted in blue) in excellent agreement with a new theoretical model accounting for axial variations and phonon self-interference (green, offset for clarity). (c) SEM measurements of the taper radius versus the offset from the taper center (blue circles) and the profile inferred from the theoreticalmodel(pinkline).AsampleSEMimageoftheopticaltaperwaistisinset.

light are coupled into the LP_{11} mode, evolving into a combination of TE_{01}, TM_{01}, and HE_{21} modes at the taper waist. The two drives then generate forward propagating phonons, and following energy and momentum conservation rules, the probe can only absorb energy from the acoustic wave and generate the anti-Stokes sideband (see also [26,30]). Generation of the Stokes sideband requires phonons propagating backwards, which are absent. The relative phase noise accumulated in the three input optical tones in the system is carefully controlled using two phase-locked loops, stabilizing (reducing) the relative frequency difference of the three optical tones to within ∼1 Hz. In addition, optical path length differences between the detected FIM-FAM signal and the LO are compensated for to avoid a frequency-dependent background that degrades the SNR [53,54]. Compensating for these sources of noise enables fW power sensitivity and the ability to resolve gain-length products (GL) at the level of $1 \times 10^{-4}\ \mathrm{W}^{-1}$ (see Supplement 1 for additional details). Note that the four-wave spectroscopy technique is convenient but not essential to the FIM-FAM interaction, which should also be observable with twofrequency techniques developed in prior Brillouin spectroscopy studies[30,41].

Frequency-resolved measurements of the anti-Stokes FIM-FAM response of the taper reveal three distinct Fano-like resonances at 134, 209, and 220 MHz [Fig. 5(a)]. These frequencies correspond precisely to those predicted by FIM-FAM interactions between the fundamental optical mode and the TE_{01}, TM_{01}, and HE_{21} optical modes, respectively [dashed lines in Fig. 5(a)]. Notably, the appearance of three distinct resonance frequencies for the same acoustic mode illustrates the frequency tunability of FIM-FAM interactions through the optical wavevector, which in this case is determined by the effective indices of the higher order optical modes. Frequency-resolved measurements of the corresponding Stokes response, in contrast, yield no resonant features, as expected for a nonreciprocal intermodal interaction [yellow trace in Fig. 5(a)]. To generate the Stokes sideband instead, either the spatial modes of the two drive fields would need to be swapped, or the probe would need to be in the other spatial mode. As expected, the resonant features are also absent when the two optical drive tones are off [orange trace in Fig. 5(a)]. The relative magnitude of the three resonances varies with the input polarization because of the polarization dependence of the MSC and the resultant variation of the relative power transferred to the higher order optical modes. For the measurements shown in Fig. 5(a), for example,thepolarizationisadjustedtomaximizetheopticalpower in the TE_{01} mode, leading to a larger response at the 134 MHz resonance. The other resonances can be optimized with alternative inputpolarizationstates(seeSupplement1formoredetails).

The optomechanical spectral measurements reveal oscillations onthelow-frequencysideofeachoftheresonantpeakfrequencies, which are neither influenced by the sweeping time duration nor the sweeping direction of the acoustic frequency ⍰. To investigate if these new optomechanical features result from the unique combination of long phonon lifetimes and axial variations in the system, we develop a theoretical model including these effects. The Brillouin interaction equations in the steady-state for the phonon amplitude (b) and measured anti-Stokes signal (a_{AS}) in thefour-wavemixingprocesscanbewrittenas

$$v_a \frac{db}{dz} = \left(-i(\Omega_0 - \Omega) + \frac{\mathbf{0}}{2}\right) b - i g_0 a_{d1} a_{d2}^{*} \qquad (1)$$

$$v_0 \frac{da_{AS}}{dz} = -i g_0 b a_p, \qquad (2)$$

where a_{d1} and a_{d2} are the drive field amplitudes, a_p is the third probe amplitude, b is the acoustic field amplitude, v_a is the acousticgroupvelocity,v_o istheopticalgroupvelocity,⍰$_0$ isthephonon resonancefrequency,$\mathbf{0}$ istheacousticdissipationrate,and g_0 isthe optomechanical coupling rate. Equation (1) describes the acoustic drive process, and Eq. (2) describes the probe scattering process. Foraxiallyinvariantsystems,theseequationsaresimplifiedbecause the phonons are strongly damped, which allows for neglecting the spatial evolution of the acoustic fields $(\frac{db}{dz} \sim 0)$, resulting in simple closed-form solutions [55]. In prior analysis of axially varying systems, the waveguide is treated as a concatenation of segments that are short enough that axial variations are negligible but long enough compared to the acoustic decay length, such that acoustic evolution can be again ignored $(\frac{db}{dz} \sim 0)$. This condition, derived in Supplement 1 $\left(\Gamma \gg \sqrt{\frac{\partial \Omega_0}{\partial z} \frac{v_a}{2\pi}}\right)$, leads to the well-known inhomogeneous spectral broadening effect [56,57]. However, in the

FIM-FAM system under investigation, with long acoustic lifetimes, these conditions do not hold (i.e., $\Gamma < \sqrt{\frac{\partial \Omega_0}{\partial z} \frac{v_a}{2\pi}}$). Therefore,Brillouinsystemswithlong-livedacousticwavesrequire amorecomprehensivetheoreticalapproach.

The formal solutions to Eqs. (1) and (2) suggest new spectral features (e.g., see Supplement 1), which we investigate further by numerically solving the equations of motion and calculating the axial dependence of the physical parameters ($⍰_0$, g_0, 0, v_a, v_o) through their dependence on the axial variation of taper radius, $r(z)$. We numerically solve Eqs. (1) and (2) by assuming that the axial variation of the taper radius is symmetric about the center ($z = z_0$) and that it follows a polynomial dependence, $r(z) = \alpha_0 + \alpha_1(z - z_0)^2 + \alpha_2(z - z_0)^4 + \ldots$. The parameter ($\alpha_j$) are determined by fitting the numerically solved spectra ($a_{as}(⍰)$) to the experimental spectra and minimizing the resulting error. Numerical analysis reveals that in this regime of fast axial variation and long phonon lifetimes, phonons undergo selfinterference, leading to qualitative coherent effects on the spectra, including broadening and broadband oscillations. Intuitively, these oscillations can be understood as long-lived acoustic waves with a frequency and magnitude given by the local geometry, interfering with acoustic waves generated in a subsequent section with a different locally determined frequency and magnitude. The local phase-matched Brillouin frequency ($⍰_0$) increases with decreasing $r(z)$, leading to a peaked response at a high frequency where the radius is minimum at the long taper waist, with a lower-frequency tail given by the gradually increasing taper transition region. No spectral oscillations appear in the measured response from the high-order acoustic modes from the same device, asexpected because the reducedlifetime from theincreased frequencyprecludesphononself-interference.

The theoretical spectrum obtained by numerically solving the Brillouin rate equations accounting for phonon self-interference [Fig. 5(b), green trace, offset for clarity] is in excellent agreement withtheexperimentalresults[Fig.5(b),bluetrace].Fromourtheoretical models, we estimate a quality factor of 2000 ± 200 and a peakgainof430 ± 40 W^{-1} m^{-1} fortheTE$_{01}$ resonance.Thisgain value is in excellent agreement with the gain predicted through the coupling calculations above. The error in the estimation primarily dependsontheerrorinestimatingthelossofthetaperfordifferent spatial modes and the precision of our numerical fitting procedure (see Supplement 1). The axial variation of the taper used in the theoretical model is validated through position-dependent SEM measurements[Fig.5(c)],displayinggoodagreement.

3. DISCUSSION

In this work, we report strong FIM-FAM interactions for the first time, inside an optical fiber taper. Here we discuss several potential implications of and improvements to these results. For example, the present tapers suffer from excess loss to the higher-order optical modes (Supplement 1 Sec. S3) [58,59] because the transition regions do not vary sufficiently adiabatically due to a length constraint of the fabrication apparatus. Therefore, future efforts could focus on increasing the transition region for truly adiabatic conversion and lower losses. Moreover, a promising alternative to theexponentialtapertransitionsimplementedinthepresentstudy is a linear transition region, which has been shown to yield low conversionlossoversmallertransitionlengths[60,61].

For many applications, a single-peaked optomechanical response is required. Therefore, the spectral structure resulting from phonon self-interference would limit the applicability of this initial taper design. However, the theory presented here predicts a strong, narrowband, and single-peaked response if the taper waist is homogeneous. A moving heater in conjunction with the present fabrication technique, for example, would yield optical tapers with a homogeneous waist. Homogeneous tapers with arbitrarily shaped transition regions and waist lengths exceeding 20 cm have been demonstrated previously [62–64]. FIM-FAM in such a device would yield very large gain-length (GL) products of around 100 W^{-1} from an ideal single-peaked and narrowband optomechanicalresonance.

The theoretical model presented here generalizes previous investigations valid under specific approximations. For example, an early analysis of FIM-FAM interactions does not include the vectorial nature of the interaction [65], a recent numerical analysis does not consider axial variations [40], and models describing optomechanical interactions in axially varying systems predict inhomogeneous broadening [56,57] but cannot access the novel spectral phonon self-interference features observed in this work for desirable long-lived acoustic waves. The model presented here is vectorial, accounts for strong axial variations, accurately describes experimental observations, and has enabled us to first identify and demonstrate the unique benefits of highly confined FIM-FAM for simultaneously achieving desirable high optomechanical coupling and long phonon lifetimes. Moreover, the comprehensive model developed here could have broader implications for the design and fabrication of high *Q* optomechanical systems. For example, the spectral variety available from phonon self-interferencemaybeleveragedfortailoringtheoptomechanical response through inhomogeneity engineering. On the other hand, unwanted consequences from phonon interference effects such as spectral broadening may modify design tolerances for fabrication inhomogeneity for some systems, such as photonic crystal fibers and on-chip hybrid waveguides. In this case, the presented model willbevaluablefordesigningsystemsresilienttoundesirableinterference effects. Finally, since the phonon interference spectrum is unique to the device geometry, phonon self-interference presents a promising new tool for extracting the geometry of axially varying optomechanicalsystemswithasinglespectralacquisition.

The presented strong single-sideband optomechanical coupling spanning new frequency and phonon-lifetime regimes has straightforward practical implications. Taper-based FIM-FAM, even this initial device, could provide orders of magnitude lifetime improvements for lifetime-limited traveling-wave Brillouin applications, including light storage, RF photonic filtering, and optical delay lines. For example, state-of-the-art traveling-wave Brillouin-optical storage devices [20] achieve ∼40-ns storage times with ∼10 ns phonon lifetime and coupling strengths of ∼ 500 $W^{-1}m^{-1}$. By implementing similar techniques, taperbased FIM-FAM, with a phonon lifetime of 2.4 μs, would present a ∼200-fold increase in storage times while retaining large desirable operation bandwidths and coupling strengths. Similarly, the Brillouin RF filters based on the backward-Brillouin interaction are limited to an intrinsic linewidth of ∼ 10 MHz [66], whereas homogeneous taper-based FIM-FAM systems with sub-100 kHz linewidths could yield

~150-times narrower tunable RF photonic filters with comparable coupling strengths[67].

The large coupling of FIM-FAM in a fiber taper stems from the strong overlap of the tightly confined optical and acoustic modes. Strong FIM-FAM interactions can also be engineered in other optical waveguides using alternative acoustic guiding mechanisms, including phononic bandgaps [68] and weak guidance techniques [69,70]. Different frequencies for FIM-FAM interactions can be implemented by tuning the relative effective indices of the participating optical modes supported through these mechanisms. By prioritizing designs with a low relative optical effective index, photonic-phononic waveguides could enable access to ~1 − 10 MHz flexural modes, with corresponding phonon lifetimes long enough to enable approaching ms storage times and kHz filter bandwidths. In addition, preliminary calculations suggest that for fixed geometry and quality factor, the flexural-mode FIM-FAM coupling strength has a strong (super-linear) inverse dependence on phonon frequency. The potential for unprecedented lifetimes (>20 μs) and coupling strengths ($>10^4$ W^{-1} m^{-1}) motivates further fundamental and application-based development of FIM-FAM processes.

This study focuses experimentally on strong FIM-FAM interactions between two specific optical modes mediated by the fundamental flexural mode. However, FIM-FAM interactions could generally involve different optical modes and/or other fundamental acoustic modes. For example, coupling calculations show that intermodal interactions between the TE_{01} and TM_{01} higher-order optical modes mediate interaction with the fundamental torsional mode in this device near 100 MHz frequencies. Engineering FIM-FAM interactions with different combinations of acoustic and optical modes could form the basis for new acoustic sensing technologies, reveal unexplored phonon dynamics, and enable new frequency-agile optomechanical devices.

4. CONCLUSION

In summary, we have demonstrated strong forward intermodal optomechanical interactions with the fundamental flexural acoustic mode (FIM-FAM) in a few-mode optical fiber taper. By combining sensitive four-wave mixing spectroscopy, spatially selective optical coupling, and a two-stage phase noise-canceling technique, we measure the FIM-FAM spectral response, including a strong phonon resonance at 134 MHz frequency, with a quality factor of 2000 and a coupling strength around 430 W^{-1} m^{-1}. Spectral measurements reveal novel phonon self-interference effects due to the combination of large axial variations and long phonon lifetimes. A comprehensive model is developed to account for phonon self-interference, which accurately models the experimental results presented and is relevant to a large class of axially varying optomechanical systems. FIM-FAM interactions feature long phonon lifetimes, strong coupling, and single-sideband amplification and represent a promising basis for a new class of high-performance and tailorable traveling-wave optomechanical devices.

Funding. National Science Foundation (ECCS-1943658); University of Rochester.

Acknowledgment. We thank Brian McIntyre and the University of Rochester Integrated Nanosystems Center for their expertise and assistance with the SEM characterization of the taper devices.

Disclosures. The authors declare no conflicts of interest.

Data availability. Data underlying the results presented in this paper are not publicly available at this time but may be obtained from the authors upon reasonable request.

Supplemental document. See Supplement 1 for supporting content.

REFERENCES

1. A. Kobyakov, M. Sauer, and D. Chowdhury, “Stimulated Brillouin scattering in optical fibers,” Adv. Opt. Photon. 2, 1–59 (2010).
2. B. J. Eggleton, C. G. Poulton, P. T. Rakich, M. J. Steel, and G. Bahl, “Brillouin integrated photonics,” Nat. Photonics 13, 664–677 (2019).
3. I. S. Grudinin, A. B. Matsko, and L. Maleki, “Brillouin lasing with a CaF2 whispering gallery mode resonator,” Phys. Rev. Lett. 102, 043902 (2009).
4. H. Lee, T. Chen, J. Li, K. Y. Yang, S. Jeon, O. Painter, and K. J. Vahala, “Chemically etched ultrahigh-Q wedge-resonator on a silicon chip,” Nat. Photonics 6, 369–373 (2012).
5. S. Gundavarapu, G. M. Brodnik, M. Puckett, T. Huffman, D. Bose, R. Behunin, J. Wu, T. Qiu, C. Pinho, N. Chauhan, J. Nohava, P. T. Rakich, K. D. Nelson, M. Salit, and D. J. Blumenthal, “Sub-hertz fundamental linewidth photonic integrated Brillouin laser,” Nat. Photonics 13, 60–67 (2019).
6. J. Geng, S. Staines, Z. Wang, J. Zong, M. Blake, and S. Jiang, “Highly stable low-noise Brillouin fiber laser with ultranarrow spectral linewidth,” IEEE Photon. Technol. Lett. 18, 1813–1815 (2006).
7. M. Merklein, B. Stiller, I. V. Kabakova, U. S. Mutugala, K. Vu, S. J. Madden, B. J. Eggleton, and R. Slavík, “Widely tunable, low phase noise microwave source based on a photonic chip,” Opt. Lett. 41, 4633–4636 (2016).
8. J. Li, H. Lee, and K. J. Vahala, “Microwave synthesizer using an on-chip Brillouin oscillator,” Nat. Commun. 4, 2097 (2013).
9. A. Motil, A. Bergman, and M. Tur, “State of the art of Brillouin fiber-optic distributed sensing,” Opt. Laser Technol. 78, 81–103 (2016).
10. X. Bao and L. Chen, “Recent progress in Brillouin scattering based fiber sensors,” Sensors 11, 4152–4187 (2011).
11. E. A. Kittlaus, P. Kharel, N. T. Otterstrom, Z. Wang, and P. T. Rakich, “RFphotonic filters via on-chip photonic-phononic emit-receive operations,” J. Lightwave Technol. 36, 2803–2809 (2018).
12. D. Marpaung, B. Morrison, M. Pagani, R. Pant, D.-Y. Choi, B. LutherDavies, S. J. Madden, and B. J. Eggleton, “Low-power, chip-based stimulated Brillouin scattering microwave photonic filter with ultrahigh selectivity,” Optica 2, 76–83 (2015).
13. Y. Stern, K. Zhong, T. Schneider, R. Zhang, Y. Ben-Ezra, M. Tur, and A. Zadok, “Tunable sharp and highly selective microwave-photonic bandpass filters based on stimulated Brillouin scattering,” Photon. Res. 2, B18–B25 (2014).
14. A. Choudhary, I. Aryanfar, S. Shahnia, B. Morrison, K. Vu, S. Madden, B. Luther-Davies, D. Marpaung, and B. J. Eggleton, “Tailoring of the Brillouin gain for on-chip widely tunable and reconfigurable broadband microwave photonic filters,” Opt. Lett. 41, 436–439 (2016).
15. M. Merklein, B. Stiller, K. Vu, S. J. Madden, and B. J. Eggleton, “A chipintegrated coherent photonic-phononic memory,” Nat. Commun. 8, 574 (2017).
16. Z. Zhu, A. M. C. Dawes, D. J. Gauthier, L. Zhang, and A. E. Willner, “Broadband SBS slow light in an optical fiber,” J. Lightwave Technol. 25, 201–206 (2007).
17. R. Pant, A. Byrnes, C. G. Poulton, E. Li, D. Y. Choi, S. Madden, B. LutherDavies, and B. J. Eggleton, “Photonic chip based tunable slow and fast light via stimulated Brillouin scattering,” in *Conference on Lasers Electro-Optics, CLEO* (2012), Vol. 37, pp. 969–971.
18. K. Y. Song, K. Lee, and S. B. Lee, “Tunable optical delays based on Brillouin dynamic grating in optical fibers,” Opt. Express 17, 10344–10349 (2009).

19. S. Preußler, K. Jamshidi, A. Wiatrek, R. Henker, C.-A. Bunge, and T. Schneider, “Quasi-light-storage based on time-frequency coherence,” Opt. Express 17, 15790–15798 (2009).
20. B. Stiller, M. Merklein, C. Wolff, K. Vu, P. Ma, S. J. Madden, and B. J. Eggleton, “Coherently refreshing hypersonic phonons for light storage,” Optica 7, 492–497 (2020).
21. M. Merklein, B. Stiller, and B. J. Eggleton, “Brillouin-based light storage and delay techniques,” J. Opt. 20, 083003 (2018).
22. E. P. Ippen and R. H. Stolen, “Stimulated Brillouin scattering in optical fibers,” Appl. Phys. Lett. 21, 539–541 (1972).
23. A. Choudhary, B. Morrison, I. Aryanfar, S. Shahnia, M. Pagani, Y. Liu, K. Vu, S. Madden, D. Marpaung, and B. J. Eggleton, “Advanced integrated microwave signal processing with giant on-chip Brillouin gain,” J. Lightwave Technol. 35, 846–854 (2017).
24. R. Pant, C. Poulton, H. MacFarlane, L. Thevenaz, D. Y. Choi, J. Steve, S. J. Madden, B. Luther-Davies, and B. J. Eggleton, “On-chip stimulated Brillouin scattering,” Opt. Express 19, 8285–8290 (2011).
25. R. M. Shelby, M. D. Levenson, and P. W. Bayer, “Guided acoustic-wave Brillouin scattering,” Phys. Rev. B 31, 5244–5252 (1985).
26. G. Bashan, H. H. Diamandi, Y. London, K. Sharma, K. Shemer, E. Zehavi, and A. Zadok, “Forward stimulated Brillouin scattering and opto-mechanical non-reciprocity in standard polarization maintaining fibres,” Light Sci. Appl. 10, 119 (2021).
27. M. S. Kang, A. Nazarkin, A. Brenn, and P. St. J. Russell, “Tightly trapped acoustic phonons in photonic crystal fibres as highly nonlinear artificial Raman oscillators,” Nat. Phys. 5, 276–280 (2009).
28. R. Van Laer, B. Kuyken, D. Van Thourhout, and R. Baets, “Interaction between light and highly confined hypersound in a silicon photonic nanowire,” Nat. Photonics 9, 199–203 (2015).
29. H. Shin, W. Qiu, R. Jarecki, J. A. Cox, R. H. Olsson, A. Starbuck, Z. Wang, and P. T. Rakich, “Tailorable stimulated Brillouin scattering in nanoscale silicon waveguides,” Nat. Commun. 4, 1944 (2013).
30. E. A. Kittlaus, N. T. Otterstrom, and P. T. Rakich, “On-chip inter-modal Brillouin scattering,” Nat. Commun. 8, 15819 (2017).
31. H. Kim and H. Shin, “Large on-chip Brillouin net amplification in siliconbased nano-photonics,” AIP Adv. 9, 125032 (2019).
32. T. R. Meeker and A. H. Meitzler, “Guided wave propagation in elongated cylinders and plates,” in *Physical Acoustics* (1964), pp. 111–167.
33. P. St. J. Russell, D. Culverhouse, and F. Farahi, “Experimental observation of forward stimulated Brillouin scattering in dual-mode single-core fibre,” Electron. Lett. 26, 1195–1196 (1990).
34. G. Bahl, M. Tomes, F. Marquardt, and T. Carmon, “Observation of spontaneous Brillouin cooling,” Nat. Phys. 8, 203–207 (2012).
35. J. Kim, M. C. Kuzyk, K. Han, H. Wang, and G. Bahl, “Non-reciprocal Brillouin scattering induced transparency,” Nat. Phys. 11, 275–280 (2015).
36. C. H. Dong, Z. Shen, C. L. Zou, Y. L. Zhang, W. Fu, and G. C. Guo, “Brillouin-scattering-induced transparency and non-reciprocal light storage,” Nat. Commun. 6, 6193 (2015).
37. R. Van Laer, R. Baets, and D. Van Thourhout, “Unifying Brillouin scattering and cavity optomechanics,” Phys. Rev. A 93, 053828 (2016).
38. J. C. Beugnot, S. Lebrun, G. Pauliat, H. Maillotte, V. Laude, and T. Sylvestre, “Brillouin light scattering from surface acoustic waves in a subwavelength-diameter optical fibre,” Nat. Commun. 5, 5242 (2014).
39. D. M. Chow, J.-C. Beugnot, A. Godet, K. P. Huy, M. A. Soto, and L. Thévenaz, “Local activation of surface and hybrid acoustic waves in optical microwires,” Opt. Lett. 43, 1487–1490 (2018).
40. M. Cao, L. Huang, M. Tang, Y. Mi, W. Jian, W. Ren, and G. Ren, “Intermode forward Brillouin scattering in nanofibers,” J. Lightwave Technol. 38, 6911–6917 (2020).
41. M. S. Kang, A. Brenn, and P. St. J. Russell, “All-optical control of gigahertz acoustic resonances by forward stimulated interpolarization scattering in a photonic crystal fiber,” Phys. Rev. Lett. 105, 153901 (2010).
42. E. A. Kittlaus, N. T. Otterstrom, P. Kharel, S. Gertler, and P. T. Rakich, “Non-reciprocal interband Brillouin modulation,” Nat. Photonics 12, 613–619 (2018).
43. M. S. Kang, A. Butsch, and P. St. J. Russell, “Reconfigurable light-driven opto-acoustic isolators in photonic crystal fibre,” Nat. Photonics 5, 549–553 (2011).
44. A. W. Snyder and J. D. Love, *Optical Waveguide Theory* (Chapman and Hall, 1983).
45. R. N. Thurston, “Elastic waves in rods and clad rods,” J. Acoust. Soc. Am. 64, 1–37 (1978).
46. R. N. Thurston, “Elastic waves in rods and optical fibers,” J. Sound Vib. 159, 441–467 (1992).
47. J. Zemanek, “An experimental and theoretical investigation of elastic wave propagation in a cylinder,” J. Acoust. Soc. Am. 51, 265–283 (1972).
48. R. A. Waldron, “Some problems in the theory of guided microsonic waves,” IEEE Trans. Microw. Theory Tech. 17, 893–904 (1969).
49. G. E. Hudson, “Dispersion of elastic waves in solid circular cylinders,” Phys. Rev. 63, 46–51 (1943).
50. W. Qiu, P. T. Rakich, H. Shin, H. Dong, M. Soljaci˘ c, and Z. Wang,´ “Stimulated Brillouin scattering in nanoscale silicon step-index waveguides: a general framework of selection rules and calculating SBS gain,” Opt. Express 21, 31402–31419 (2013).
51. H. Zhang, W. Pang, H. Yu, and E. S. Kim, “High-tone bulk acoustic resonators on sapphire, crystal quartz, fused silica, and silicon substrates,” J. Appl. Phys. 99, 124911 (2006).
52. C. Krischer, “Optical measurements of ultrasonic attenuation and reflection losses in fused silica,” J. Acoust. Soc. Am. 48, 1086–1092 (1970).
53. A. Iyer, W. Xu, J. E. Antonio-Lopez, R. A. Correa, and W. H. Renninger, “Ultra-low Brillouin scattering in anti-resonant hollow-core fibers,” APL Photon. 5, 096109 (2020).
54. L. E. Richter, H. I. Mandelberg, M. S. Kruger, and P. A. McGrath, “Linewidth determination from self-heterodyne measurements with subcoherence delay times,” IEEE J. Quantum Electron. QE-22, 2070–2074 (1986).
55. R. W. Boyd, *Nonlinear Optics* (Academic, 2020).
56. V. I. Kovalev and R. G. Harrison, “Observation of inhomogeneous spectral broadening of stimulated Brillouin scattering in an optical fiber,” Phys. Rev. Lett. 85, 1879–1882 (2000).
57. C. Wolff, R. Van Laer, M. J. Steel, B. J. Eggleton, and C. G. Poulton, “Brillouin resonance broadening due to structural variations in nanoscale waveguides,” New J. Phys. 18, 025006 (2016).
58. S. Ravets, J. E. Hoffman, L. A. Orozco, S. L. Rolston, G. Beadie, and F. K. Fatemi, “A low-loss photonic silica nanofiber for higher-order modes,” Opt. Express 21, 18325–18335 (2013).
59. M. C. Frawley, A. Petcu-Colan, V. G. Truong, and S. Nic Chormaic, “Higher order mode propagation in an optical nanofiber,” Opt. Commun. 285, 4648–4654 (2012).
60. T. A. Birks and Y. W. Li, “The shape of fiber tapers,” J. Lightwave Technol. 10, 432–438 (1992).
61. C. Baker and M. Rochette, “A generalized heat-brush approach for precise control of the waist profile in fiber tapers,” Opt. Mater. Express 1, 1065–1076 (2011).
62. C. K. Ha, K. H. Nam, and M. S. Kang, “Efficient harmonic generation in an adiabatic multimode submicron tapered optical fiber,” Commun. Phys. 4, 173 (2021).
63. D. Lee, K. J. Lee, J. H. Kim, K. Park, D. Lee, Y. H. Kim, and H. Shin, “Fabrication method for ultra-long optical micro/nano-fibers,” Curr. Appl. Phys. 19, 1334–1337 (2019).
64. N. Yao, S. Linghu, Y. Xu, R. Zhu, N. Zhou, F. Gu, L. Zhang, W. Fang, W. Ding, and L. Tong, “Ultra-long subwavelength micro/nanofibers with low loss,” IEEE Photon. Technol. Lett. 32, 1069–1072 (2020).
65. P. St.J. Russell, D. Culverhouse, and F. Farahi, “Theory of forward stimulated Brillouin scattering in dual-mode single-core fibers,” IEEE J. Quantum Electron. 27, 836–842 (1991).
66. R. Pant, D. Marpaung, I. V. Kabakova, B. Morrison, C. G. Poulton, and B. J. Eggleton, “On-chip stimulated Brillouin scattering for microwave signal processing and generation,” Laser Photon. Rev. 8, 653–666 (2014).
67. S. Gertler, N. T. Otterstrom, M. Gehl, A. L. Starbuck, C. M. Dallo, A. T. Pomerene, D. C. Trotter, A. L. Lentine, and P. T. Rakich, “Narrowband

microwave-photonic notch filters using Brillouin-based signal transduction in silicon," Nat. Commun. 13, 1947 (2022).

68. P. Dainese, P. St.J. Russell, G. S. Wiederhecker, N. Joly, H. L. Fragnito, V. Laude, and A. Khelif, "Raman-like light scattering from acoustic phonons in photonic crystal fiber," Opt. Express 14, 4141–4150 (2006).
69. J. D. Dai, V. Winkel, J. E. B. Oliveira, and C. K. Jen, "Analysis of weakly guiding cladded acoustic fibers of hexagonal crystal symmetry," IEEE Trans. Ultrason. Ferroelectr. Freq. Control 39, 722–729 (1992).
70. A. Safaai-Jazi, G. W. Farnell, and C. K. Jen, "Analysis of weakly guiding fiber acoustic waveguide," IEEE Trans. Ultrason. Ferroelectr. Freq. Control 33, 59–68 (1986).